LASER INTERFEROMETER GRAVITATIONAL WAVE OBSERVATORY
- LIGO -
CALIFORNIA INSTITUTE OF TECHNOLOGY
MASSACHUSETTS INSTITUTE OF TECHNOLOGY

Technical Note	LIGO-T1700283–v1	2017/09/23

Characterization of Test Mass Scattering

SURF Student: Jigyasa Nigam, Mentors: Gautam Venugopalan, Johannes Eichholz

California Institute of Technology
LIGO Project, MS 18-34
Pasadena, CA 91125
Phone (626) 395-2129
Fax (626) 304-9834
E-mail: info@ligo.caltech.edu

Massachusetts Institute of Technology
LIGO Project, Room NW22-295
Cambridge, MA 02139
Phone (617) 253-4824
Fax (617) 253-7014
E-mail: info@ligo.mit.edu

LIGO Hanford Observatory
Route 10, Mile Marker 2
Richland, WA 99352
Phone (509) 372-8106
Fax (509) 372-8137
E-mail: info@ligo.caltech.edu

LIGO Livingston Observatory
19100 LIGO Lane
Livingston, LA 70754
Phone (225) 686-3100
Fax (225) 686-7189
E-mail: info@ligo.caltech.edu

http://www.ligo.caltech.edu/

Acknowledgements

The work done under the aegis of the LIGO SURF Program would have been incomplete without the support of my mentors Gautam Venugopalan, Johannes Eichholz who lended their support and motivation and were wonderful sources of motivation! I am also really grateful to Prof. Rana Adhikari who not only helped me envision the goals of the project but also stirred me to keep working towards them! Thank you for helping me open my eyes to new steps of opportunity and strength. Special thanks to Joseph Betzweiser (LLO) and Jameson Rollins for being patient with my questions and going out of their way to help me learn! I will forever be grateful for your guidance and kindness.

This list would be incomplete without a mention of all members of the LIGO Scientific Collaboration(LSC), the LIGO SURF Program who have all played a key role in enriching this experience. I would like to thank the SURF community, the Student Faculty Programs Office and California Institute of Technology for facilitating this program.

I am at loss of words to thank Indian Institute of Space Science and Technology and all my colleagues for enabling me to undertake my project with LIGO, Caltech.

Contents

List of Figures

List of Tables

1   Introduction

Based on Einstein's General Theory of Relativity, gravitational waves which were once just a prediction, have now been successfully detected due to the precision that Advanced LIGO (aLIGO) has been able to achieve. The detection is not, however, merely a confirmation of the theory, but it opens up the world to a new regime of gravitational physics which would provide a novel perspective of the universe, complementing the current repository of knowledge. The discovery of gravitational waves ensued years of technical innovations aided by revolutionary advances and successful realizations of theories in mathematical and physical sciences, many aimed at resolving the difficulties associated with detecting their extremely small amplitude. The Michelsons interferometer employed in the aLIGO set up is able to detect at such low amplitudes on account of many modifications that it has undergone to increase its sensitivity. The intensity of the recombined light is a function of the differential arm length (DARM) of the interferometer, and therefore, the intensity of the light at the detection port is proportional to the infinitesimal gravitational wave strain. The reliability of the setup to discern the minute fluctuations in intensity is on account of the increased stability of the laser used which is about a 100 million times more stable than an ordinary laser and has an output power of 30 W. The improved stability implies that the laser output is consistent and resistant to intensity noise. The increased stability is attained by reducing beam's natural frequency variations and power fluctuations through a series of feedback mechanisms. The fused silica test mass optics for aLIGO are about 34 cm in diameter and weigh about 40 kg to keep the radiation pressure noise to a level comparable to the suspension thermal noise. The beam spot size is sufficiently large so as to reduce thermal noise contributions.

While undergoing specular reflection, light reflects with the angle of reflection equal to the angle of incidence. Scattering is the deflection of light from this path defined by specular reflection and is mainly caused by irregularities of the reflecting surface. The scattering of light has dual demerits, firstly this scattered light can reflect off other objects in the setup and couple back into the instrument, adding noise and secondly,the light power that is lost to scattering leads to a lower signal-to-noise ratio in the interferometer. Therefore, in order to increase aLIGOs sensitivity to gravitational waves, light scattering must be reduced. According to the fundamental laws of geometric optics, light incident perpendicular to the mirror surface should retrace its path. As, ideally, no light deviates from this path, an observer trying to view the beam spot at an angle shouldn't be able to see it. Practically, however, the beam spot can be observed from different angles, although the intensity of the beam spot might vary when observed along different directions. Hence as a part of the laser beam scatters or deviates from the path governed by specular reflection on account of scatter from the test mass surface, the beam spot as observed at different angles is found to be of different intensities. This is modeled by the Bidirectional Reflection Distribution function (BRDF). [2]

$$BRDF = \frac{P_s/\Omega}{P_i cos(\theta)} \tag{1}$$

where P_i is the incident intensity, P_s is the scattered power reaching the camera sensor and Ω is the solid angle. In the course of this project, we aim to install GigE cameras to image the surface of the test masses and analyze these images to quantify light scatter by means of BRDF of the test masses.

2 Imaging with a CCD Camera

CCDs were invented in 1969 by Willard Boyle and George E.Smith at AT&T Bell Labs and they quickly took over as the preferred detector for astronomical observation. Boyle and Smith received the Nobel Prize in Physics(2009) for this revolutionary work. CCDs are now most commonly employed as detectors over a wide range of wavelength range from the near-IR to X-rays for they offer numerous benefits over other methods for imaging. Made of semiconducting silicon, CCDs use the photoelectric effect to detect photons which makes them very efficient. Performance is characterized by quantum efficiency which is a function of wavelength being employed for observation. Hence, for instance, InGaAs sensors perform much better than Si at a wavelength of 1 micron. Their high efficiencies and relatively low noise, a wider wavelength response and improved linear response are a few factors responsible for their increasing popularity. CCDs are embedded with a system of electrodes called gates allowing applied voltages to be placed on each pixel. This creates localized potential wells where electrons are trapped after they are liberated by an incoming photon.At the end of the exposure, the electrons collected in each pixel are read out: they are shifted across the CCD, the collected charge is amplified and converted to a digital number (ADU) with an analog-to-digital converter. Figure 1 shows a comparison of the responses and quantum efficiencies (Equation 2) of various imaging instruments. The use of CCDs might be limited

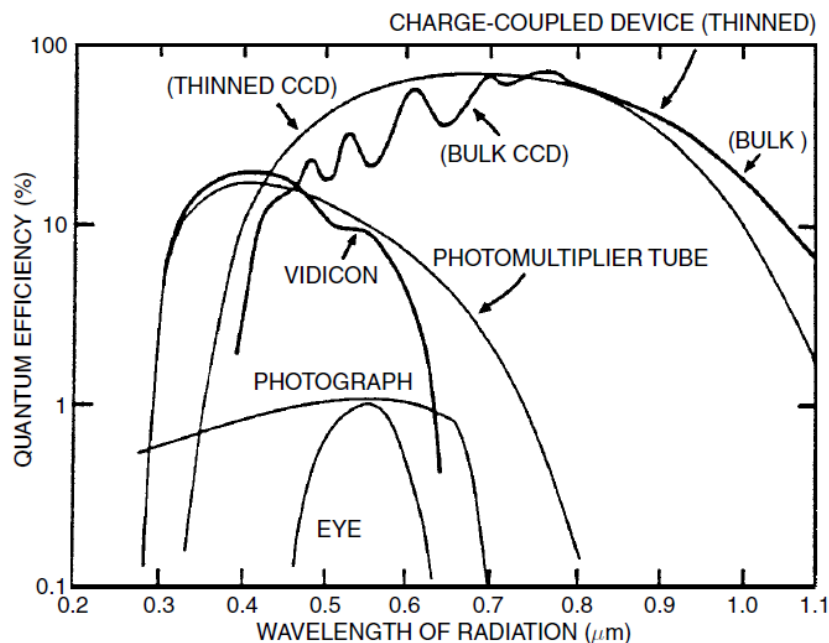Figure 1: Comparison of Quantum Efficiency.Figure courtesy of *Handbook of CCD Astronomy* [3]

due to some of the following factors including increased sensitivity to unwanted light sources, their ability to be easily saturated leading to bleeding of charge onto another pixel in the vicinity; non-uniform response caused by small variations in manufacturing and non linearity in response due to saturation.

3   Specification of the Basler ace acA640-120gm GigE camera

The camera used for the purpose of this project is the Basler ace acA640-120gm. It is equipped with a Gigabit Ethernet(GigE) interface in addition to a 6 pin Hirose connector. The GigE interface is employed for connecting to the camera which provides a framework for high speed transmission of data over ethernet network thereby increasing the speed of response, improved control over camera settings and returns the captured images to a computer so as to enable a faster and even real time data acquisition and computation. The specifications of the camera are listed below.

Table 1: Camera Specifications

Sensor	Sony ICX618
Quantum Efficiency	59% at 545 nm
	7% at 1064 nm
Temporal Dark noise	11 electrons per pixel
	at zero exposure
Saturation Capacity	16.6 ke$^-$ per pixel
CCD Sensor Type	CCD Progressive Scan

The sensitivity of a CCD sensor is governed by its quantum efficiency(QE) which is the the number of electrons generated per each incident photon. QE is a wavelength or photon energy dependent function and is also dependent on the thickness of the silicon that intercepts the incoming photons. The plot in figure 2 depicts the variation of quantum efficiency of the CCD sensor with wavelength. The original plot as provided in the sensor's data sheet was extrapolated in the range of 1 to 1.1 micron.

$$\text{Quantum Efficiency} = \frac{\text{Number of carriers or electrons generated}}{\text{Number of incident photons}} \tag{2}$$
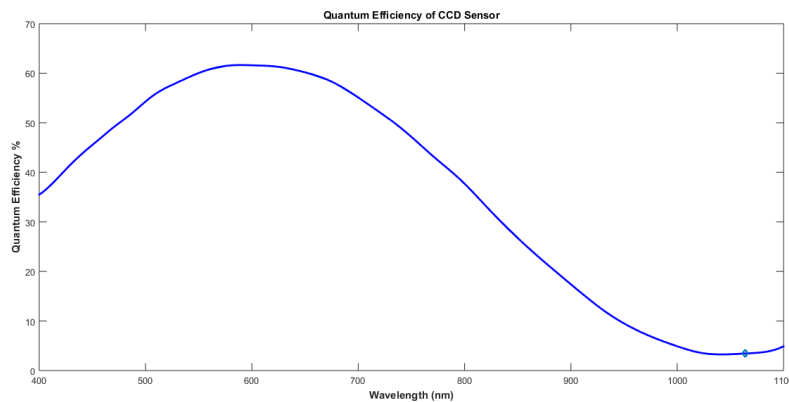

Figure 2: Quantum Efficiency of the camera sensor extrapolated beyond 1000 nm

4   Readout Mechanism employed in the sensor

Figure 3 shows, schematically, how the charges accumulated during the exposure are read out of the sensor to the image buffer. This section provides an overview of charge readout mechanism in addition to summarizing how the data is transmitted over the ethernet network.

Charges are transported from the sensors light-sensitive elements (pixels) to the vertical shift registers while charges from the bottom row of pixels in the array are moved into a horizontal shift register. Next, the charges are shifted out of the horizontal register and are converted to voltages proportional to the magnitude of each charge. Each voltage is amplified by a Variable Gain Control (VGC) and digitized by an Analog-to-Digital converter (ADC). After each voltage has been amplified and digitized, it passes through an FPGA into an image buffer. [10] This continues until all image data has been read out of the sensor. The pixel data leaves the image buffer and passes to an Ethernet controller where it is assembled into data packets to be transmitted via the Ethernet network to a network adapter in the host computer. The Ethernet controller also handles transmission and receipt of control data such as changes to the cameras parameters. The image buffer between the sensor and the Ethernet controller allows data to be read out of the sensor. As the amount of charge generated by incoming photons exceeds the sensor capacity, the CCD saturates and charge leaks from one pixel to another resulting in bright vertical streaks through an effect called *blooming*. Evidently, this affects image analysis. The readout mechanism is associated with some inaccuracies and this induces a readout noise in the images as well.
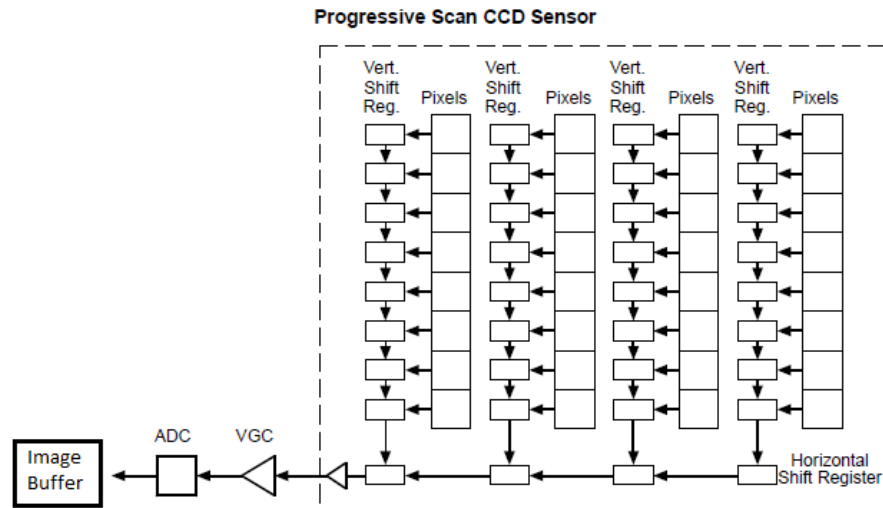

Figure 3: Readout Mechanism in the sensor

5   Telescope Design

A two lens telescope system with two biconvex lenses was envisioned for the purposes of focusing the beam spot onto the camera sensor while ensuring optimum utilization of the

CCD pixel array. The following describes the physical formalism of imaging through the telescope. The process of imaging through several optical elements can be described by the
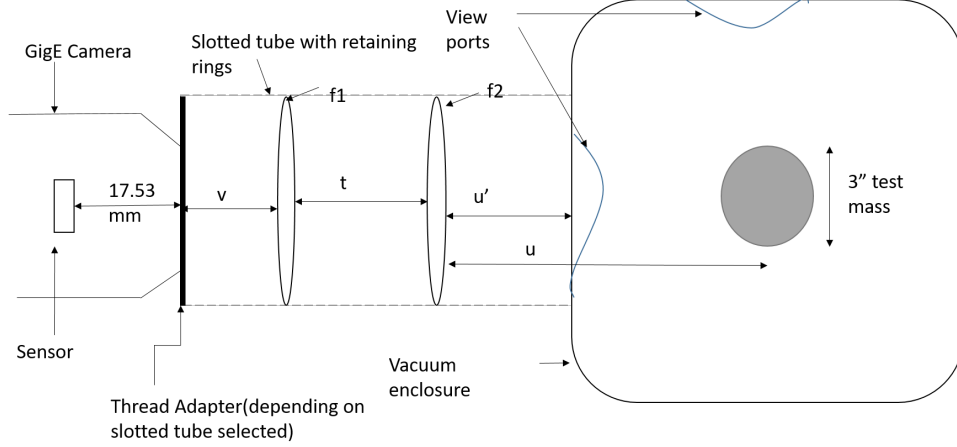

Figure 4: Schematic of the telescope design

ABCD formalism of geometrical optics wherein the 2×2 matrix is known as the system matrix. [9]

$$\begin{bmatrix} A & B \\ C & D \end{bmatrix}$$

The system matrix elements relates the ray parameters, namely its height and angle with respect to the principal axis at the input and output planes. A relates the ray height at image plane to that at the object plane given given. B relates the ray height at image plane to the angle of the ray with the principal axis at the object plane. C relates the angle which the ray at the image plane makes with the principal axis to the ray height at object plane. D relates this angle to the angle at the object plane. This formalism is employed to compute the focal length of a combination of two lenses placed a certain distance apart. Subsequently this lens combination is used for obtaining an image of the test mass which acts as the object and an image is obtained. To use the Gigabit Ethernet(GigE) camera for imaging, it is necessary that the image plane of the lens combination lies on the sensor.

The required effective focal length can be determined by multiplying the following matrices and noting that the system matrix element C is representative of the effective focal length of the two lens system, $C = -\frac{1}{f}$

$$\begin{bmatrix} y \\ y' \end{bmatrix} = \begin{bmatrix} 1 & v \\ 0 & 1 \end{bmatrix} \begin{bmatrix} 1 & 0 \\ -1/f_1 & 1 \end{bmatrix} \begin{bmatrix} 1 & d \\ 0 & 1 \end{bmatrix} \begin{bmatrix} 1 & 0 \\ -1/f_2 & 1 \end{bmatrix} \begin{bmatrix} 1 & u \\ 0 & 1 \end{bmatrix} \begin{bmatrix} x \\ x' \end{bmatrix} \tag{3}$$

where f_1 and f_2 are the focal lengths of required lenses, x and y are object and image height respectively, x' and y' represent the angles made by the ray with the principal axis.[5]

The system matrix, M, which relates the object and image parameters hence reduces to

$$M = \begin{bmatrix} 1 & v \\ 0 & 1 \end{bmatrix} \begin{bmatrix} (1 - d/f_2) & d \\ (-1/f_1 - 1/f_2 + d/f_1 f_2) & (1 - d/f_1) \end{bmatrix} \begin{bmatrix} 1 & u \\ 0 & 1 \end{bmatrix}$$
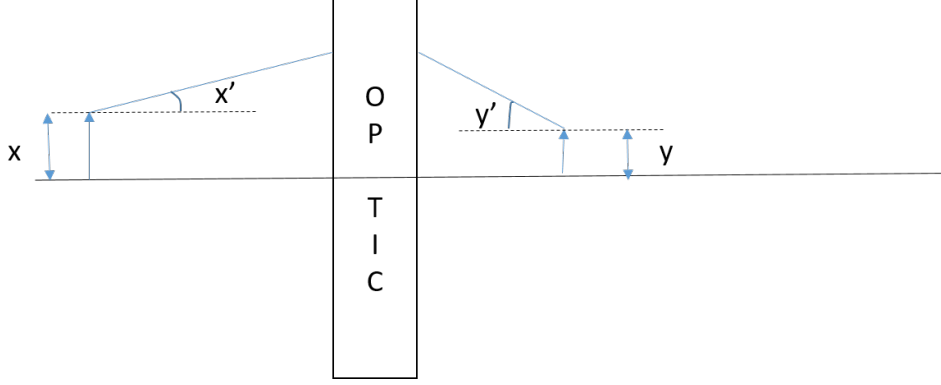
Figure 5: Imaging with ABCD formalism

Thus the effective focal length is given as $1/f = 1/f_1 + 1/f_2 - d/f_1 f_2$
The imaging in this system can be thought of as an object placed at a distance u from the system of two lenses and the image plane at a distance v from the system.

$$\begin{bmatrix} 1 & v \\ 0 & 1 \end{bmatrix} \begin{bmatrix} A & B \\ C & D \end{bmatrix} \begin{bmatrix} 1 & u \\ 0 & 1 \end{bmatrix}$$

which, on explicit multiplication, yields

$$\begin{bmatrix} A + Cv & u(A + Cv) + B + Dv \\ C & Cu + D \end{bmatrix} \tag{4}$$

The imaging condition imposed is such that light rays incident, irrespective of the incident input angles in paraxial approximation, converge to the same image plane. This sets the imaging criteria to be

$$Au + Cuv + B + Dv = 0 \tag{5}$$

$$v = \frac{-Au - B}{Cu + D} \tag{6}$$

Additionally, the relation between the output and input height becomes

$$\text{image height} = (A + Cv) \times \text{object height} \tag{7}$$

due to the restriction on the determinant of the imaging matrix, hence

$$A + Cv = \frac{1}{Cu + D} \tag{8}$$

gives the magnification. The required magnification for the image circle size 6 of $\frac{1}{4}$ inches and the object size ranging from 3 inches for the surface of the entire optic to 1 inch for focusing on the beam spot lies between 0.068 to 0.18. The optimum image circle diameter has been used for this calculation for at this diameter, the image circle just encloses the sensor and efficiently utilizes the pixel array. At an image circle size greater than this value, the entire image will not be captured and some information will be lost whereas with image circle diameter less than this value, image circle would not cover the sensor entirely and
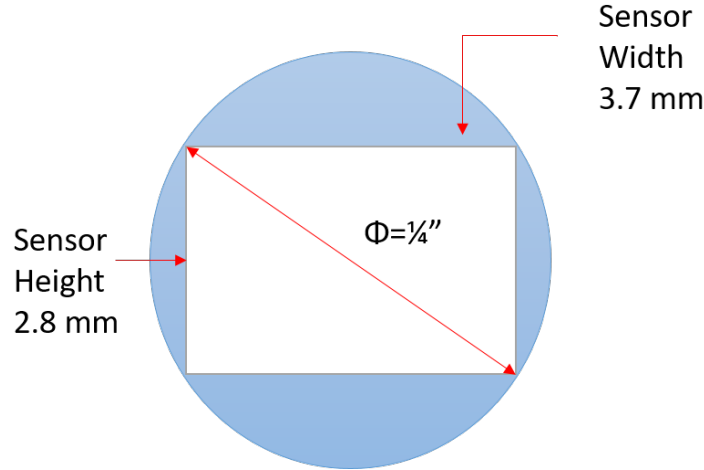
Figure 6: Image Circle enclosing the CCD sensor

therefore lead to pixel wastage as not all pixels would be utilized for imaging. With the above algorithm, a Python program was developed to optimize the focal length selection with the available options of 50, 100, 150, 200, 250, 300 mm. A sensitivity analysis on the available combination choices was also performed and it was found that an error of 1cm in fixing the object distance and 5 mm in setting the distance between the lenses would yield an error less than 1.5% in the calculated magnification. The scatter plot 7 shows the percentage error in magnification with the 150-150 mm lens combination as object distance, u, is varied over 700 to 1500 mm and for each u, as t varies from 1 to 100 mm. The next plot 8 shows the same for the lens 250-250 mm lens combination. Each point in the scatter plot shows the percentage error in magnification associated with each of the object distance, given that there is an error associated with the measurement of t and u. Each u is tested for t in the range of 0 to 100mm, hence for each u, there are 100 points in the plot, each representing the error in magnification computed if t and u were to be chosen for imaging.

Of the available diameters of the lenses, 1" and 2", lenses with diameter 2" were selected in order to ensure that the telescope is able to collect sufficient light power. The light gathering power of a lens scales proportionally with its area[20] and therefore varies directly as the square of the diameter. Hence a 2" lens is able to collect four times the light collected by a 1" lens. The lenses would ideally be AR coated for a broad range of wavelengths encompassing 532 and 1064 nm to minimize light scattering back into the interferometer and also to enable maximum transmission at these wavelengths. Due to limited focal length options in the coated 2" optics, the use of 1" lens for the second (eyepiece) lens was examined as it would give a greater flexibility in the choice of focal lengths. However the differing sizes of the lenses puts an additional constraint on the separation between them so that the light cone emerging from the first lens passes entirely through the second lens without any loss of light.

$$tan(\theta) = \frac{h_1}{v} = \frac{h_2}{v-t} \tag{9}$$

Here h_1 is limited to a maximum of 1" and h_2 is limited to 0.5". This puts a restriction on t such that t>v/2.

Figure 7: Percentage Error in 150mm- 250mm focal length combination.Individual vertical arrays of points at a given u denote a scan in t, the distance between the two lenses.
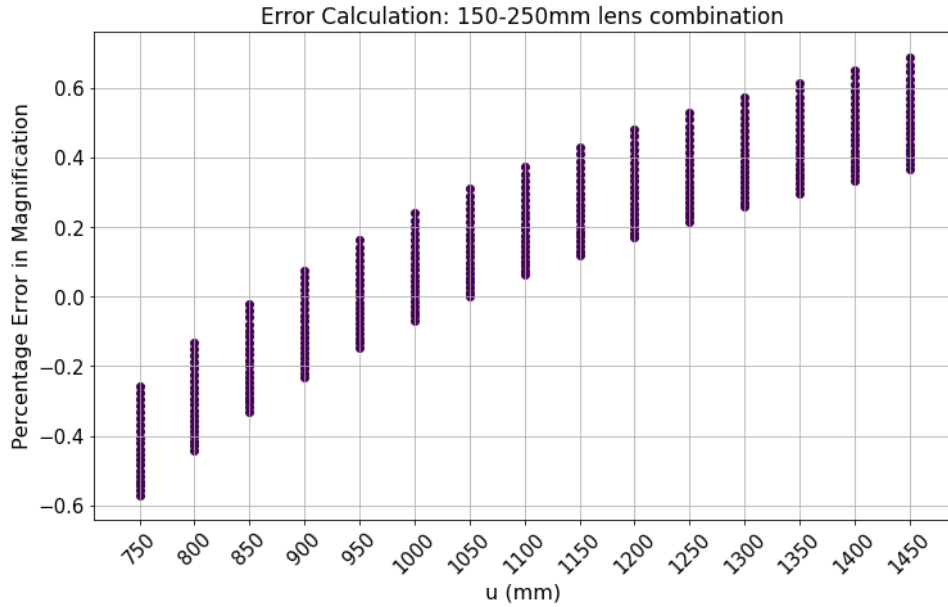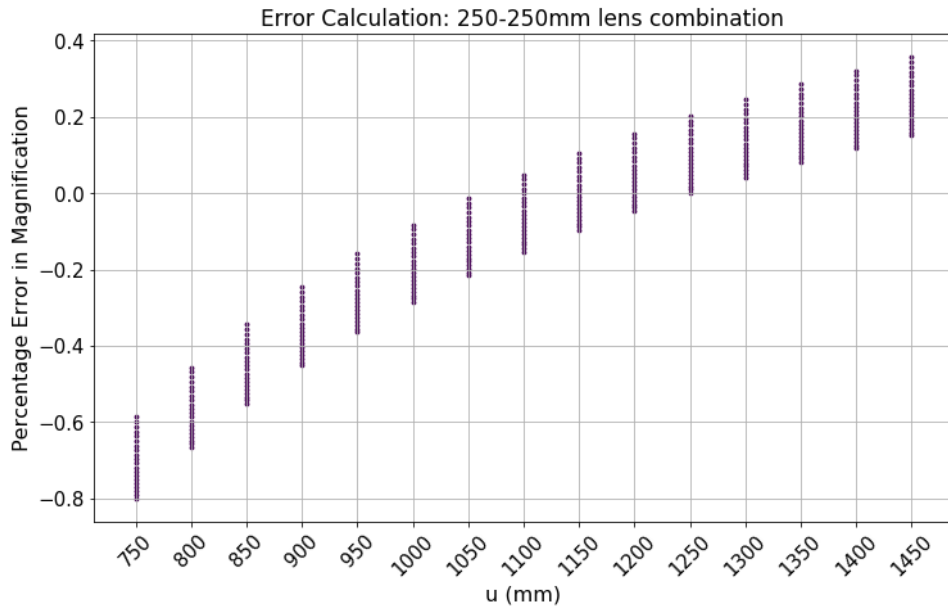

Figure 8: Percentage Error in 250mm- 250mm focal length combination.Individual vertical arrays of points at a given u denote a scan in t, the distance between the two lenses.
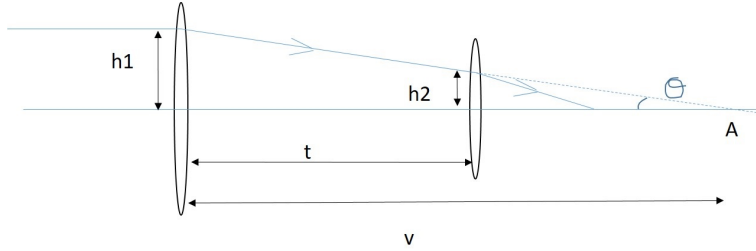
Figure 9: Telescope design with 1 inch eyepiece.

Lenses used in telescopes are characterized by their f-numbers which is calculated as

$$\text{f} - \text{number} = \frac{\text{focal length}}{\text{diameter- of- the- lens}} \tag{10}$$

The selection of 150 and 250mm 2" lenses makes the f numbers of the lenses involved to be 2.95 and 4.92 respectively. This makes the system susceptible to coma and spherical aberrations. Conventionally [19] f numbers greater than 5 have been associated with more efficient imaging where the effects of spherical aberrations are less apparent.

Rays traversing in off axis regions produce varying transverse magnification leading to coma. This effect is more pronounced when the rays from the object enter the lens at an oblique angle causing the image to be off axis. [21] The resulting shape of the image distorted by
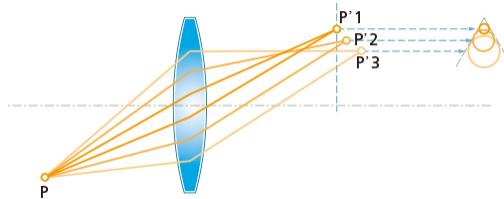
Figure 10: Coma aberration

comatic aberration resembles that of a comet with its tail, hence the name coma. The use of aspherical lenses [11] in addition to plano convex lenses was investigated however these would greatly limit the accessible object and image distances and hence we chose to make the first imaging trial with biconvex lenses.

Initially, while the procedure to procure the lenses and various components to assemble the telescope were in effect, the GigE was equipped with an available commercial Rainbow 50mm[17] lens and Basler's camera software Pylon was used to interface with the camera. By manually adjusting the aperture size and focus of the camera, a few images of objects in the control room of the lab, at distances ranging from 75cm to 1.5m were captured. The camera was then installed inside the interferometer area using a Power over Ethernet(PoE) injector connected to the Martian network switch and was installed to focus on a mirror in the mode cleaner MC2. A Power over Ethernet(PoE) connection is one wherein a single

connection over ethernet cables provides both power and a connection for data transmission. This reduces the number of connections and complexity of the network. Several images at exposure levels varying between 30 and 10000 μseconds were captured. Two of these pictures are included below in figure 11, the first captured at 300 μseconds exposure time and the second captured at an exposure time of 1000 μseconds. With the image processing code being developed, the images captured at different exposure times could be combined to obtain a high dynamic range (HDR) image which would overcome the problems of saturation and offer a better image quality .

300 μs   1000μs
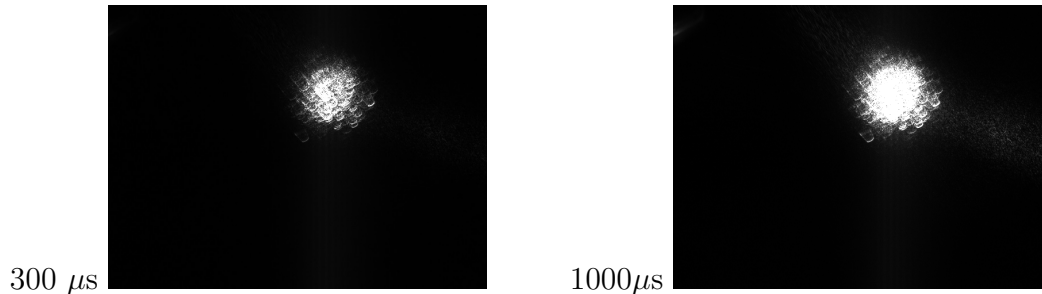
Figure 11: MC2 beam spot at 300 and 1000 microsecond exposures

6   GigE configuration

Three configuration models [1] for the GigE have been proposed which connect the camera to a computer network. While the first model 12a just involves connecting the camera directly to a PC with Pylon installation using a Power over Ethernet(PoE) connector, it would be only efficient in the basic IP configuration of the camera without involving a complex network. The second model 12b describes the integration of the camera to "Martian", the network system used in the 40m lab. The third model 12c combines the creation of a separate camera subnetwork and integrating this network with the main network in the lab through a network switch. This model would be more efficient to employ as the number of cameras increases.
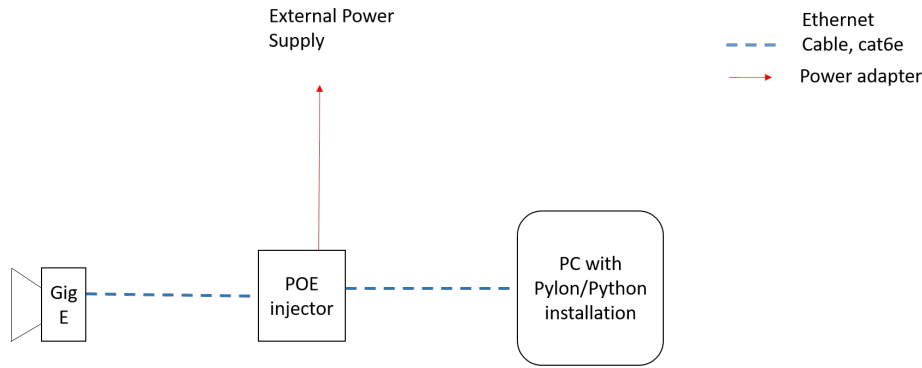
Model 1: Establishing a direct connection between the GigE and the operating PC

(a) Model 1
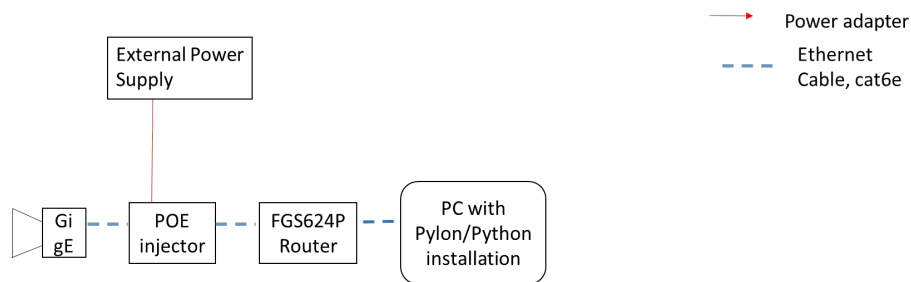
Model 2: GigE with connection via router to PC

(b) Model 2
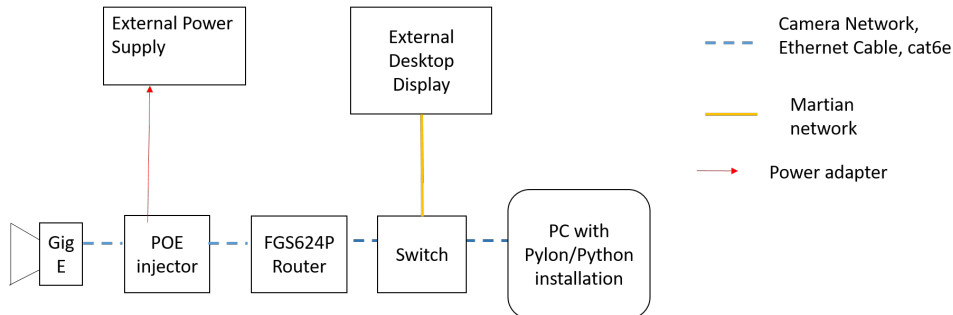
Model 3: GigE with router and main switch to connect to external display

(c) Model 3

Figure 12: GigE Network Configurations

7 High Dynamic Range Imaging(HDR)

Often the image captured by a camera does not match the actual image that would be seen by a human eye. This so happens on account of the eye's ability to continuously readjust to capture sensitive information, while the camera just captures the frame without accounting for any of the dynamic brightness gradients or contrasts among other features. Dynamic

range is the ratio between the maximum and minimum values of a physical measurement. In terms of camera terminology, it is the ratio of the intensity that just saturates the camera to the intensity that just lifts the camera response above dark noise, or simply the ratio of intensity corresponding to the brightest region of the image and the darkest. The Appendix of this report links to the Python program developed for creating HDR images. This algorithm superimposes images captured at various exposure times onto one another after scaling them with the appropriate factor which has been identified as the ratio of exposure times. It replaces the saturated pixel on one image with the unsaturated pixel of the other image being superposed. This eliminates saturation in the image to a large extent. This algorithm differs from the commonly employed tone-mapping algorithms which control the brightness and contrast of the image and are more concerned with adapting the final image content for view on a display device by uniformly scaling the pixel values, thereby limiting the image in terms of dynamic range and color gamut.[8] A High Dynamic Range(HDR) image, therefore, would resolve the contrast and image details much better than an ordinary image which might be limited by pixel saturation.

The plot in figure(13b) depicts the image histogram for an image of the ETMX captured at 14 ms exposure. The image was scaled by a factor of 1000 to enable comparison with the HDR image.

(a) ETMX at 14 ms exposure

(b) Image Histogram of a 14 ms exposure
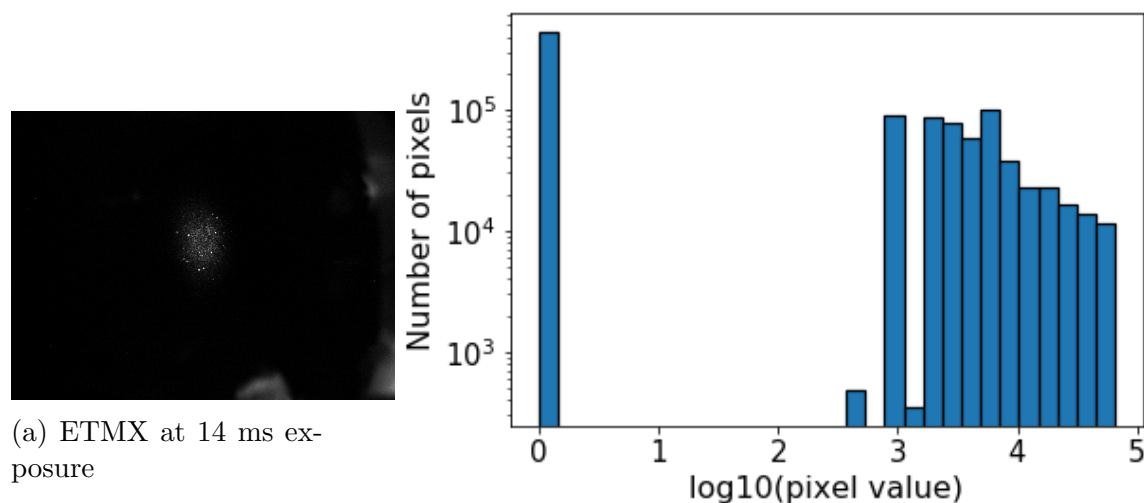
Note the x axis in the graph below(Figure13b) is in logarithmic scale. After running the HDR algorithm through a series of images of the same scene captured at different exposures, the resulting 2D image matrix in Python had floating point values. This was scaled(multiplied) by a factor of 1000 to eliminate floating points to visualize the actual spread in pixel values. Then the logarithm of pixel values was computed and plotted. Since the pixel values have been scaled by a factor of 1000, the log scale varies from 0 to 5. Clearly, the pixel values extend for a larger range and the image a greater intensity distribution.

(a) HDR image of ET-MX

(b) Image Histogram of HDR image
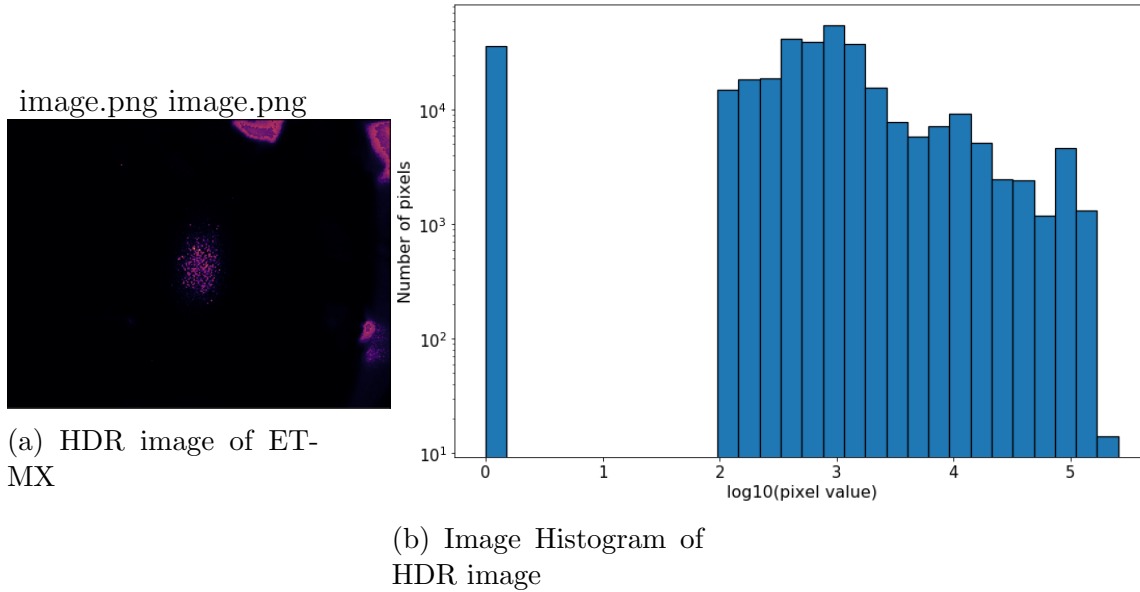
7.1 Quantifying HDR

Although the algorithm produces an image which controls saturation, it is necessary to verify if indeed the image is indeed HDR and is actually able to account for subtler differences in intensities. One possible way to examine this is by considering the bit depth of the pixels, which the range of integer values that a pixel can assume while being used for imaging. For instance, a bit depth of 8 corresponds to pixel values in the range of 0 to 255. In general, a bit depth of n corresponds to a range of values from 0 to 2^n. Clearly, higher the value of n, the larger the range of values that a pixel can assume. More on this can be found in Section 8.

The bit depth of the images captured by the camera is a parameter which can be controlled while operating the camera. It can either be set to 8 or 12. The HDR image produced by the algorithm uses several images captured at this bit depth at different exposures, however, captures a finer subtlety in intensity. This is made possible if the pixels can assume a larger range of values. In effect, this implies that the algorithm produces an image which has a higher bit depth. One proposed way to determine the bit depth of the HDR image is by plotting image histogram which is a graphical representation of the tonal distribution in a image, that is it plots the number of pixels for each pixel value. An image histogram(in figure 13b) of the image captured by the camera depicts how the pixels are being utilized inefficiently at both low levels of saturation as well as highly saturated images. The resulting HDR image however has a wider tonal distribution.(Figure 14b)

8 Image Formats

Determining the type of image format depends on three factors, namely, image size, compression and transmission speed and which one is given higher priority over the others. For imaging in LIGO, it is preferred that most of the information captured from the surface of the test masses is preserved to enable accurate scatter measurements. The various types of

Table 2: A glance at the different image formats

BMP	Outdated image format
GIF	Most useful for animation, logos, single tones
JPEG	Lossy Compression, variety of RGB combination
TIF	International Standard for scientific imaging , Lossless compression(LZW, ZIP algorithms)
PNG	Lossless compression, alpha channel to superimpose images

available image formats are distinguished by the amount of compression. Files are generally compressed to reduce the amount of memory space they occupy and this compression is achieved by either a lossy means or a lossless one. Lossless compression utilizes some compression algorithms such as LZW[18], ZIP among others to reduce file size while retaining all information in the original image file. Lossy compression on the other hand selectively discard image data which is deemed to be, visually, less significant. JPEG compression is an example of a lossy compression algorithm used in .jpg images. To minimize distortion associated with compression or compression artifacts, lossy compression should be used only in the last step, after all image editing and analysis has been completed. Of the available image formats namely GIF, JPG, BMP, TIFF, PNG; PNG and TIF are more commonly used in scientific imaging and applications requiring image processing.

- BMP(Bitmap Image File) format is quite old and not very relevant for modern usage as it is pixel dependent and generally does not allow compression.

- GIF is mostly used for animation and is ideal for images such as logos, cartoons which have large areas of single tone colors without much variations in intensities. Clearly this would not be suitable for imaging the test mass due to intensity variations in the image.

- JPEG(Joint Photographic Experts Group) is the most widely used image format today. It offers about 16.7 million colors, each color(RGB) has a bit depth of 8 bits giving a total bit depth of 24 and hence the multitude of colors.The amount of compression is dependent on image content, for images with higher noise levels or detail are not as easily compressed with monotone content.

- PNG(Portable Network Graphics) files employ lossless compression to reduce file size and support compositing, that is, images with transparent background can be imposed on top of another and used as its background.

- TIFF (Tagged Image File Format) is a portable format, accessible with a variety of programs offers the ability to store multiple images in one file.The TIFF format allows the editing and resaving of the image without suffering a compression loss. Hence it is often used for storing images that need to be edited and re-saved. They can have a bit depth of 8 or 16 bits per color channel and this would offer higher flexibility. The figure 15 below illustrates a comparison between the black and white color gradients

obtained with 8 bits and 16 bits. TIFF is an international standard for storing and interchanging bitmaps between applications and hardware platforms.
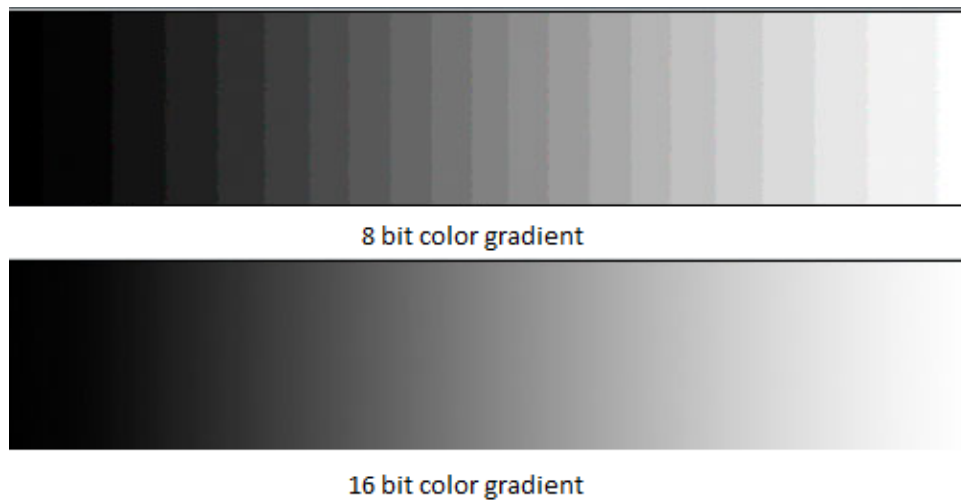

Figure 15: Color gradients with a bit depth of 8 bits and 16 bits

The TIFF files can be compressed to save memory and increase speed of transmission while preserving image quality. There are three compression methods- LZW, ZIP both of which are lossless and JPEG compression which is lossy. While compression comes with these added advantages, it might make the file slower to work with and also hamper its compatibility. TIFF preserves IPTC(International Press Telecommunications Council) metadata and has tags which store the information about the type of compression used and also gives developers a chance to apply for their own private tags which could include information about the organization and the project. The standard for storing astronomical images is the FITS ('Flexible Image Transport System) Astronomical Data Format. It has been endorsed by NASA and the International Astronomical Union. It is commonly used for the transport, analysis, and archival storage of scientific data sets, processing 1D spectra, 2D images and multidimensional data cubes. The FITS format is compatible with the AstroPy (Python) and Matlab.

8.1   Compression algorithm

This section describes the compression algorithm employed most commonly for compressing .TIF files. LZW [14] is a "dictionary"-based [15] compression algorithm which implies that LZW encodes data by referencing a dictionary. Thus, to encode a substring, only a single code number, corresponding to that substring's index in the dictionary, needs to be written to the output file. Dictionary based algorithms scan a file for sequences of data that occur more than once. These sequences are then stored in a dictionary and within the compressed file, references are put wherever repetitive data occurred. LZW starts out with a dictionary of 256 characters as the "standard" character set. It reads data 8 bits at a time and encodes the data as a number that represents its index in the dictionary. Each instance of a new

substring is added to the dictionary. For each substring that has already been encountered in the past, a new character is read and concatenated with the current string to get a new substring. This substring is encoded using a single number. Usually a maximum number of entries is defined for the dictionary to preserve memory.

9 Image Acquisition at ETMX

The GigE camera was installed at ETMX (End Test Mass X) which focuses on the optic at an angle. A few pictures of the beam spot were captured at various exposures ranging from 14 ms to 0.5 s.This exposure time is a significant increase over the exposure used at MC2, primarily because most of the laser light undergoes specular reflection and a very small fraction of the intensity is reflected to the CCD sensor which is observing the test mass at an angle of approximately 40 degrees.

Figure 16: Beam Spot on ETMX

10 Overview of CCD Calibration

There are multiple techniques to image with a CCD, each with its own set of unique characteristics. The standard method of CCD imaging is to point the camera to a particular location and integrate with the detector for a specified amount of time. On achieving the required integration time, the CCD is readout. Another method is *drift scanning*, which consists of reading the exposed CCD at a slow rate while simultaneously mechanically moving the CCD itself to avoid image smear. Another variation of this technique is time delay integration, which is more relevant to astronomy as the CCD does not move at all but is readout at exactly the sidereal rate (to track objects in transit). For imaging the test mass, the camera is fixed onto the mount and the standard method of varying the exposure time

to capture images is used.

The images captured by a CCD are subject to noise which can be reduced by properly using calibration images. The use of the basic set of calibration images in the reduction of CCD object frames is as follows.

Dark frames are images taken with no light so that pixel values arise only due to bias and dark current. About 10 dark images are captured after acquiring data frame with other settings unchanged. These are stacked to build a master dark frame. A flat field is an image of a uniformly illuminated surface. Any deviation from absolute homogeneity is due to CCD or optical imperfections. Everything about the optical set-up (type of projection, focus) should be as used for the light Frames to be calibrated. Averaging a number of dark frames and flat fields minimizes the quantum noise. For each data or light frame, the master dark frame is subtracted from it and divided by the master flat frame. As each dark frame contains the bias, it is subtracted from the light frame during dark frame subtraction. These steps correct the object frame for bias level, dark current and non-uniformity within each image pixel.

11 Need of CCD Radiometric Calibrations

11.1 Terminology Review

Table 3: Terminology Review

Flux ϕ	The optical power or rate of flow of radiant energy. It represents the total radiation emitted by a source or transmitted through a surface or impinging upon a surface. Dimensionally, it is measured in Watts.
Irradiance	Measure of flux per unit area striking a surface. Radiant exitance is a terminology u for the flux per unit area leaving a surface. Since the surface element can be oriente at any angle towards the direction of the beam, these quantities do not indicate anything about the directionality of the flux.
Radiance, L	Accounts for the intensity of optical radiation emitted or reflected from a certain location on an emitting or reflecting surface in a particular direction. Mathematicall it is the flux per unit solid angle per unit projected area of the source or surface. The projected area is defined as the projection of the area vector onto a surface norr to the direction of view and is equal to the actual area times the cosine of the angle between the surface normal and the direction of view. Radiance can vary with position on a surface and with direction.
BRDF Equation1	The ratio of the scattered radiance to the incident irradiance.

Radiometric calibration is the process of mapping sensor measurements to a physical quantity. While employing a CCD camera to make quantitative power measurements the recorded pixel values must be decoded as radiance. The opto-electronic conversion function which maps physical power to a pixel value varies for each pixel both because of manufacturing variations in the CCD elements themselves (or fixed-pattern noise) and due to variations in

the radiance at each pixel due to the slightly different solid angles subtended by the extended light source at each pixel. This is depicted in the figure 17 Hence, radiometric calibration is used to characterize the variations in the conversion function across the image.
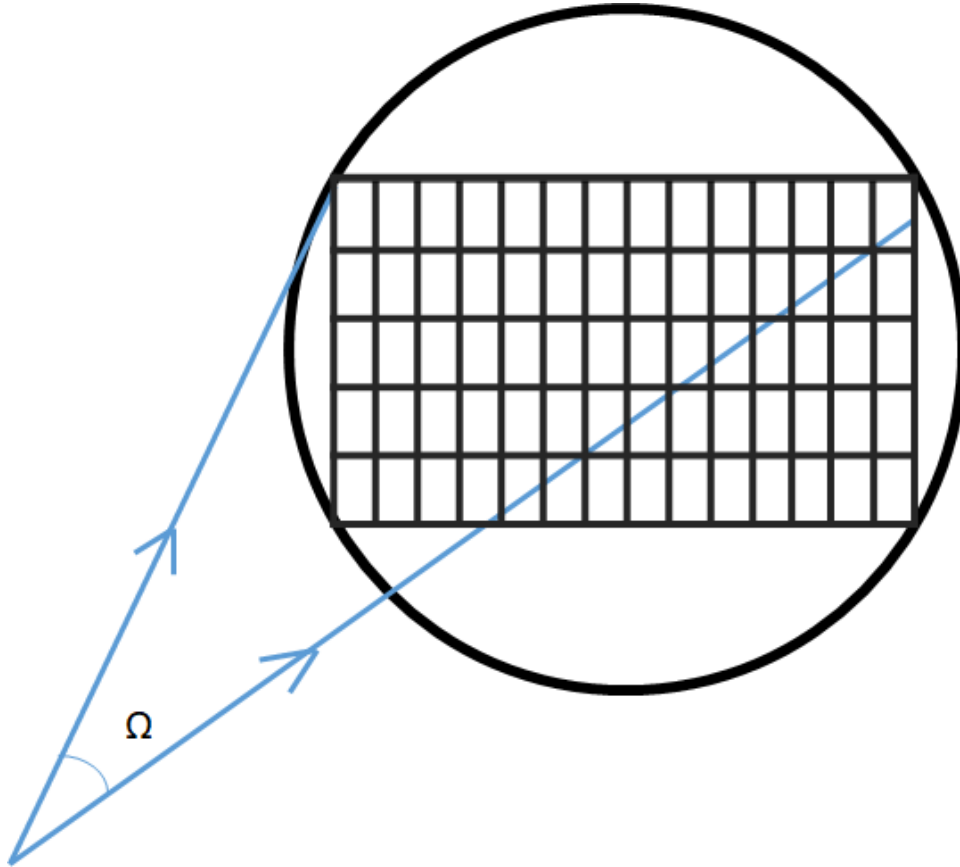

Figure 17: Pixel array in image circle with each pixel experiencing a different solid angle.

12   Linearity of CCD Response

A CCD sensor records the intensity of incoming light photons in terms of pixel counts which is representative of the number of electrons emitted from the sensor. The image as a two dimensional array contains these pixel counts. The pixel values depend on the pixel format used for imaging. While a pixel format of 8 bits can have values ranging from 0 to 255, a 16 bit pixel stores values within 0 and 65535. Clearly a wider range of pixel values means that a pixel can record intensity variations to a greater degree as explained in the section on HDR imaging. 7 However, the function which maps the pixel values to incident power is linear only up to saturation. If pixels saturate, the additional light that hits the sensor is not registered in the image and hence power estimation algorithms yield inaccurate data. In the linear regime of operation, a CCD response is modelled as the following.

$$\frac{\text{Pixel Count}}{\text{Exposure}} \times \text{CF} = \text{Power(in W)} \tag{11}$$

$$\text{CF} = \text{Power(in W)} \times \frac{\text{Exposure}}{\text{Pixel Count}} \tag{12}$$

where CF is the Calibration Factor of the camera which is representative of the scaling of power that happens in the sensor due to the gain or loss during sensor readout and conversion of charge accumulated on a pixel to ADU. The saturation capacity of the CCD sensor puts a limit on the incident power density on the sensor. When operated on the continuous shot mode, the GigE camera captures frames at a frame rate specified by the exposure time for the shot. For instance, the following is a calculation for a frame rate of 103.3 frames/second. The pixel is in the shape of a square with a side of 5.6 μ m. The power incident on a pixel (P_{pixel}) is related to the saturation incident intensity (I_{sat}) and the area of a pixel as follows.

$$P_{pixel} = I_{sat}.A_{pixel}$$

$$P_{pixel} = \frac{n_{sat}}{QE_\lambda}\frac{h_p c}{\lambda}.frame\_rate$$

where A_{pixel} is the area of a pixel, n_{sat} is the saturation capacity of the pixel(in number of electrons), QE_λ is the quantum efficiency of the sensor at incident wavelength λ and h_p is the Planck's constant, c is the speed of light in vacuum. Substituting λ=1064nm, QE_λ=6%, and n_{sat} as 16.6 ke$^-$, the saturation incident power density is computed to be 0.145639 W/m^2 Assuming that the incident laser beam is uniformly spread over the sensor, would imply a beam diameter of 1/4" or 4.5 mm, yielding a saturation incident power of 2.31989 μW. For the purposes of this project, the linearity of response was tested although quantitative values relating power and pixel values were obtained by radiometric calibrations described in the next section.
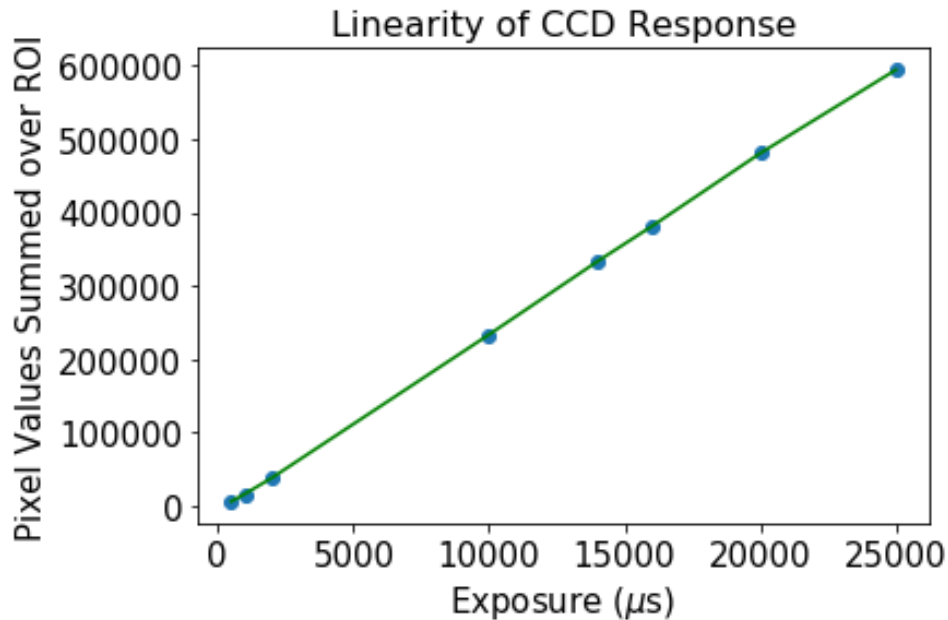

Figure 18: Linearity of CCD Response, computed from white paper test at 60°

The graph 18 shows linear response recorded by the CCD sensor as the exposure time was increased between successively captured pictures.

13   CCD Calibration for BRDF measurements

In order to relate irradiance onto a surface to the radiance towards the detector, the reflectance properties of the material must be examined. The reflectance properties are a function of incoming and outgoing angle, wavelength, polarization, and position. Restricting the parameters to angles, a function known as the Bidirectional Reflectance Distribution function(BRDF) gives a suitable measure of the scatter. To interpret a pixel value as a measurement of BRDF, the response of the pixel sensor to radiance, irradiance due to the light source at the relevant surface point the geometric arrangement of the surface normal, the viewing direction and illumination direction must be known. The reflecting surfaces, on the basis of BRDF, can be classified into distinct categories[7]. Lambertian Model which models the surface as a diffuse reflector, has a symmetric BRDF, that is, its BRDF is independent of the angle of incidence or the angle of reflection and has a constant value of $\frac{1}{\pi} sr^{-1}$. Phong, Ward, Lafortune and Torrance-Sparrow models are also well known empirical BRDF models among others. On the basis of mathematical fitting, BRDF models have been classified in terms of the orthogonal bases functions which include spherical harmonics, wavelets among others. However modelling scatter in this space might rely on many coefficients for a good approximation and hence rarely used. These models are however limited to opaque surfaces which are isotropic in roughness, so reflectance is invariant under a rotation about the surface normal. Surfaces with very small roughness are similar in behavior to perfectly smooth surfaces, but their specular reflectance is attenuated.

To calibrate the camera for BRDF measurements and verify if there's any angle dependence to imaging, it would be ideal to use a Lambertian scatterer which has a uniform reflectance irrespective of angle of incidence.

A study[4] to characterize white papers on the basis of BRDF measurements, examines a set of 8 papers glossy paper (G), semi-glossy paper (SG), matte coated paper (MC) and paper for plain photocopies (PPC) and 4 Japanese papers or washi. The papers were classified into rough (PPC, MC) and smooth(G and SG). Based on observations at 284 combinations of incident and observing angle in the specular reflection plane, it was concluded that MC showed an almost constant Lambertian-like diffuse reflection and would come the closest to an ideal Lambertian surface followed by printing paper. The papers used for the study were MC- Seiko Epson MJA4SP1; PPC- NBS Ricoh, 90-1312

Given an incoming light direction, w_i, and an outgoing reflected direction, w_o, each defined relative to a small surface element. BRDF is defined as the ratio of the quantity of reflected light in direction wo, to the amount of light that reaches the surface from direction w_i. If the quantity of light reflected from the surface in direction w_o is labeled as L_o, and the amount of light arriving from direction wi, E_i. Then BRDF is given by

$$\text{BRDF} = \frac{L_o}{E_i} \tag{13}$$

Comparing the images captured by a CCD at different angles to the power meter readings, for an arbitrary fixed angle of incidence would help verify the accuracy of the measurements.
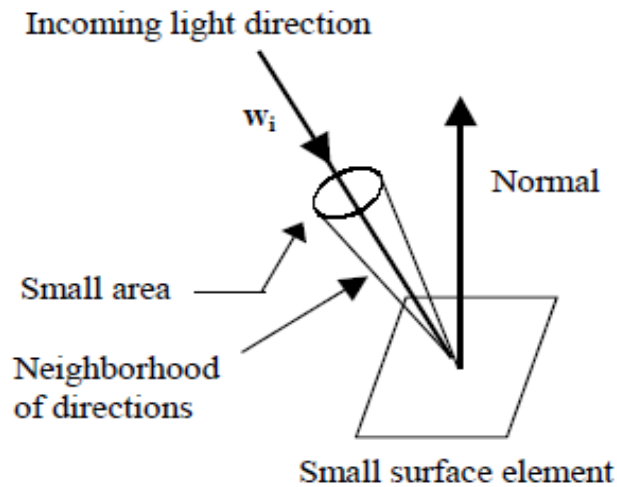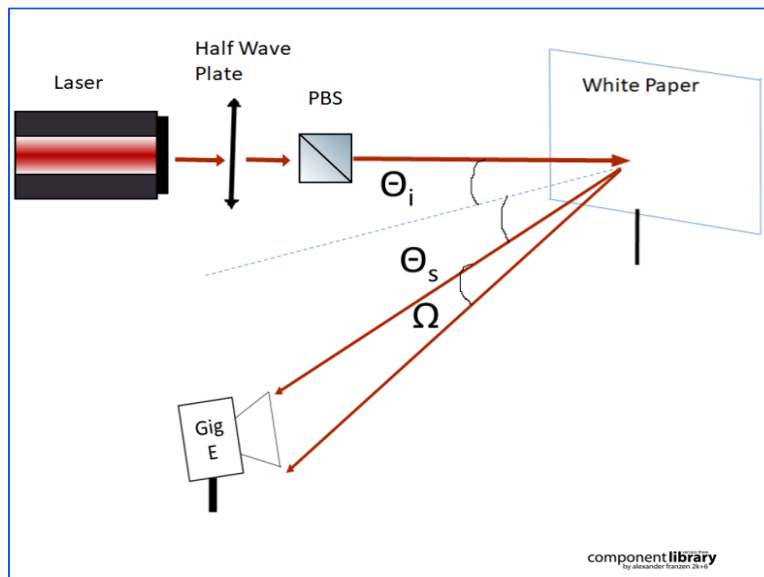
Figure 19: BRDF

13.1 Procedure

Figure 20: BRDF

The setup in figure 20 describes the procedure for calibrating the CCD to radiometric response and for further BRDF measurements. A 1064nm laser (150 mW, preferably linearly polarized) is required for the setup. In case the linearly polarized laser is not available, a quarter wave plate (QWP) is used to alter the polarization state of the light. The linearly polarized light is passed through a HWP and a PBS(90-10) to control the incident power. A photodiode can monitor the reflected power and give an estimate on the incident power on

the sample. (Although not used here, the beam may be passed through a telescope system with two lenses to magnify the spot size and then through an iris to top hat the beam and ensure uniform illumination). The paper sample is mounted at a fixed arbitrary angle to the beam to maintain a constant angle of incidence. Images of the beam spot on the paper are captured at different exposures at a given observation angle, while also recording the input laser power and the scattered power with a power meter. Subsequent measurements are taken by changing the observation angle at an interval of 10 degrees and repeating the measurement. ND filters may be placed before the camera to prevent saturation.
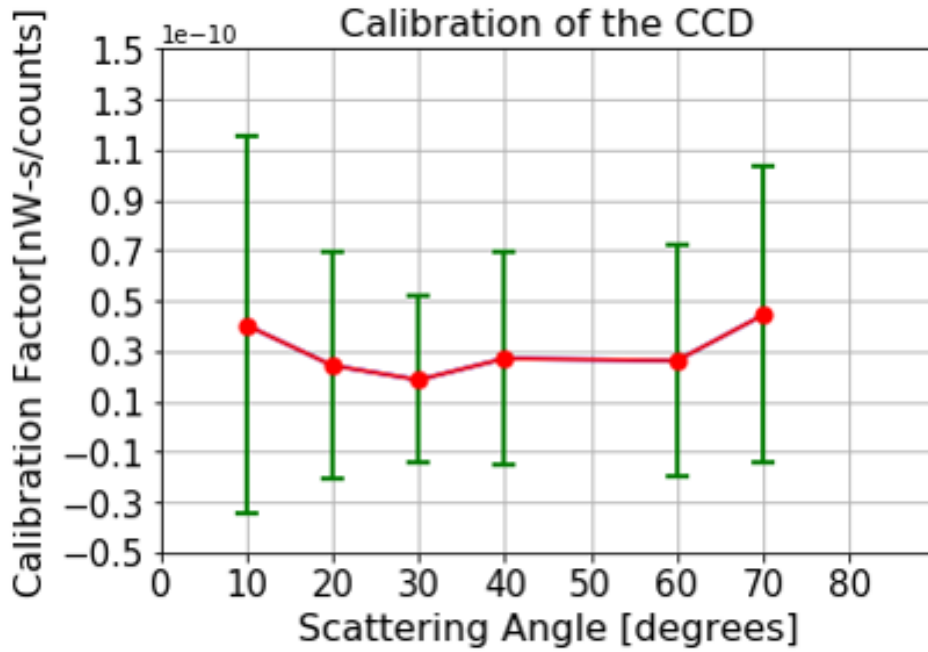
13.2   Analysis

Figure 21: Calibration factor of the CCD

A region of interest(RoI) centered around the beam spot was selected in each of the images. Through a Python script, the pixel values over the RoI were summed and divided by the corresponding exposure time. A constant BRDF of $\frac{1}{\pi}$ was assumed for the Lambertian scatterer. Known the scattering angle and the incident power, the scattered power was calculated according to the following equation

$$P_s = BRDF \times P_i \times cos(\theta_s) \times \Omega = \text{Calibration Factor (CF)} \times \frac{\sum\limits_{RoI} \text{Pixel Value}}{\text{Exposure time}} \qquad (14)$$

Thus the scattered power was calculated and so was the calibration factor. The calibration factor was observed to be constant over the variation in angle.

14 MC2 Loss Map

The pitch and yaw offsets of the Wavefront Sensor (WFS) in the mode cleaner(MC2) were varied randomly to values confined between -0.5 and 0.5 and the corresponding transmitted intensity was observed. A surface plot of the transmission intensity versus the pitch and yaw offsets values was obtained using a Python code. It identifies the pitch and yaw offsets which would correspond to maximum transmission and which would correspond to the least. It is hypothesized that the areas of minimum transmission are prone to maximum scatter loss. The scatter plot figure 22 shows a plot of the intensities recorded on varying the offset angles.
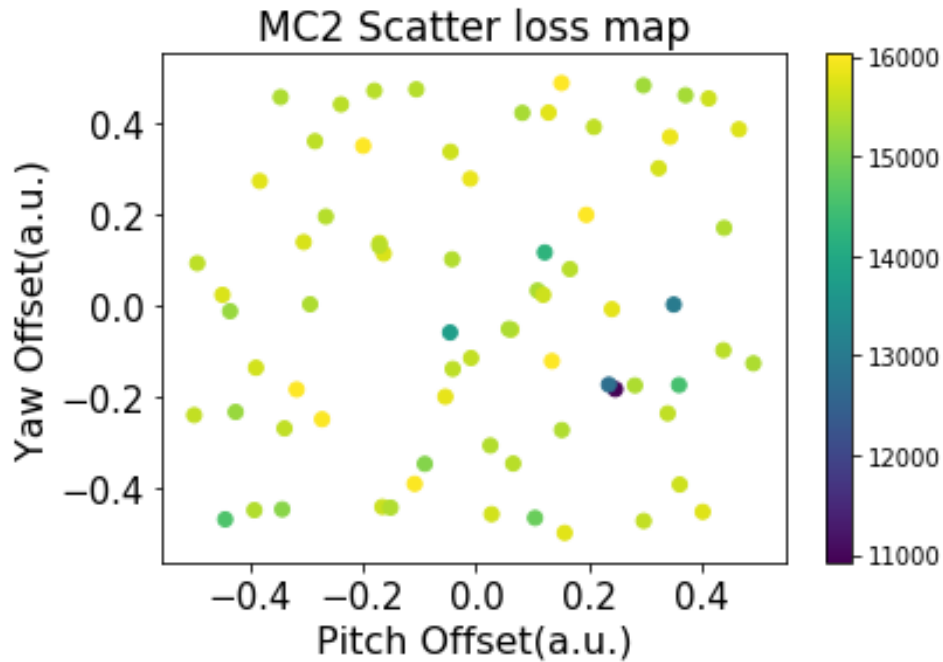

Figure 22: Uncalibrated MC2 scatter map

The figure below 23 shows a surface loss map of MC2 plotted with another set of interpolated observations. The uncolored circles represent the data points. The radial scale is in arbitrary units since the data is uncalibrated.
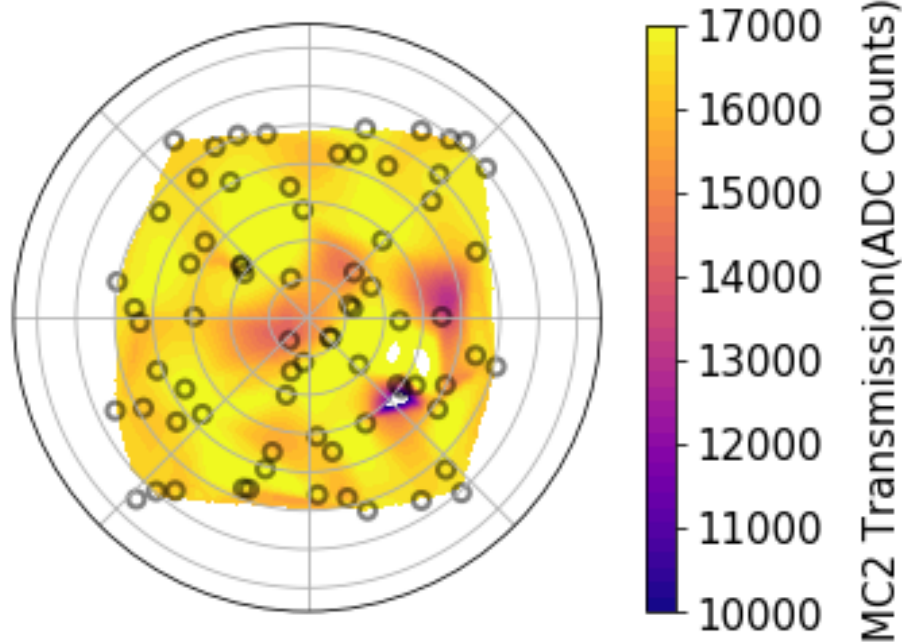
Figure 23: MC2 surface loss map

15   Future Work

- The project could be taken up further to establish a dedicated camera server network as discussed in section 6. This network could then be connected to the local Martian.

- Additionally, the proposed two inch telescope system could actually implemented and replace the commercial lens being currently employed.

- The concept of point scattering could be examined in much greater detail along with potential causes and mitigation strategies and a more quantitative relation between the number of point scatterers and contributed noise could be established.

- MC2 loss map could be calibrated to relate the change in offset to a physical length(in mm) that the beam moved across the face of the test mass.

- Explore methods to capture a live video feed from the camera to observe the real time movement of point scatterers on the surface of the test mass. Although the use of OpenCV, ffmpeg and gstreamer was partially explored, programs such as Aravis [16] could be employed.

- The images captured by the camera could also be redirected to the CRT monitors in the control room via DVI to VGA adapters. These adapters connect the CRT monitor to the LCD screen computer requesting data from the camera.

Appendix

Various codes in Python and C were developed over the duration of the project.

- Python Code for HDR imaging

- Python Code for Loss Map characterization of MC2 test mass

- C Program to establish communication with the camera and adjust camera parameters

- C Program for Single Shot and Continuous Shot Operations

- Python program with PyPylon to operate the camera using EZCA channels

- Python program to identify point scatterers in the image
  These may be found at https://github.com/CaltechExperimentalGravity/GigEcamera

References

[1] Joseph Betzweiser, Michael Thomas *aLIGO GigE Camera Layout and Usage* Technical Note LIGO-T1300202-v1, 2015

[2] Fabian Magana-Sandoval, Rana Adhikari, Valera Frolov, Jan Harms, Jacqueline Lee, Shannon Sankar, Peter R. Saulson and Joshua R. Smith *Large-angle scattered light measurements for quantum-noise filter cavity design studies.* Technical Note LIGO-T1400252-LSC.(2014)

[3] Steve B Howell, *Handbook of CCD Astronomy*, Cambridge University Press(2006)

[4] Yoshinori Akao, Norimichi Tsumura, Toshiya Nakaguchi and Yoichi Miyake *Characterization of white paper sheets by BRDF model parameters estimated in the specular reflection plane* Journal of Imaging Science and Technology 54, no. 6 (2010): 60503-1.

[5] Bastian Schwarz ; Gunnar Ritt ; Michael Koerber ; Bernd Eberle *Laser-induced damage threshold of camera sensors and micro-optoelectromechanical systems* Opt. Eng. 56(3), 034108, Mar 20, 2017

[6] Prabal Nandy, Kurtis J. Thome, Stuart F. Biggar, *Characterization and field use of a C-CD camera system for retrieval of bidirectional reflectance distribution function* Journal of Geophysical Research, Vol. 106, No. Dll, 11957-11966, June 16, 2001

[7] Stephen H. Westin, Hongsong Li, and Kenneth E. Torrance, *A Comparison of Four BRDF Models*, Cornell University Program of Computer Graphics, Eurographics Symposium on Rendering, April 2004

[8] G. Eilertsen, R. K. Mantiuk, J. Unger, *A comparative review of tone-mapping algorithms for high dynamic range video* , Eurographics, Volume 36 (2017), Number 2

[9] Ajoy Ghatak, *Optics.*4th Edition (2009)

[10] Basler ace User manual for GigE cameras, Basler Document Number AW000893, 31 October 2016

[11] Fundamental Optics www.cvimellesgriot.com

[12] http://www.qsimaging.com/ccd_noise_measure.html

[13] http://astro.physics.uiowa.edu/~srs/29137_09/ccd-RLM.pdf

[14] http://microscopy.duke.edu/fileformats.html

[15] www.cse.nd.edu/~cseprog/proj99/final/files/aviderga.lzw.doc

[16] www.github.com/TheImagingSource/tiscamera/wiki/Aravis

[17] http://scemosystems.fi/en/rainbow-g50mm-11-8-lens-with-cs-mount-50mm-f1-8-16-closed

[18] https://users.cs.cf.ac.uk/Dave.Marshall/Multimedia/node214.html

[19] http://old.observers.org/beginner/eyepieces.freeman.html

[20] http://www.astronomynotes.com/telescop/s6.htm

[21] http://www.azooptics.com/Article.aspx?ArticleID=660

[22] http://www.qsimaging.com/ccd_noise_measure.html